JOURNAL OF COMPUTATIONAL PHYSICS **138,** 302–330 (1997)
ARTICLE NO. CP975820

A Lagrangian Vorticity Collocation Method for Viscous, Axisymmetric Flows with and without Swirl

J. S. Marshall* and J. R. Grant†

*Department of Mechanical Engineering and Iowa Institute of Hydraulic Research, University of Iowa, Iowa City, Iowa 52242; †Naval Undersea Warfare Center, Newport, Rhode Island 02841

Received March 12, 1996; revised June 10, 1997

This paper presents a new Lagrangian vorticity collocation method for viscous, axisymmetric fluid flows with or without swirl. The velocity calculation is performed using a representation of the vorticity field in terms of Gaussian vortex rings for off-center points and Gaussian vortex blobs along the axis of symmetry. A matrix equation for the element ''amplitudes'' is obtained via a collocation approach, by fitting the vorticity representation to the known vorticity values at the control points, prior to each velocity evaluation. This matrix equation is solved using an iterative procedure, which both speeds the calculation and filters out ''noise'' in the element amplitudes. Viscous diffusion is accomplished with use of a diffusion velocity method, in which control points are moved with the sum of the local fluid velocity and an additional ''diffusion velocity'' that accounts for the effect of viscosity on the spread of vorticity support. Derivatives are obtained by locally fitting a polynomial function to control points about a given control point via a least-square formulation and then differentiating the polynomial. This method is found to maintain high accuracy even for very irregularly spaced control points. The method introduced for viscous diffusion in the paper can also be used for three-dimensional vortex methods in general.

Key Words: vortex methods, collocation, Navier–Stokes equations, diffusion

1. INTRODUCTION

Axisymmetric fluid flows, both with and without swirl, are an attractive choice in modeling a wide variety of fluid flow phenomena, since they offer the resolution of two-dimensional flows but exhibit many of the physical effects associated

0021-9991/97 $25.00

with vorticity stretching and re-alignment of more general three-dimensional flows. Axisymmetric flows are frequently employed, for instance, to model problems involving flame dynamics, thermal plumes, bluff-body wakes, and axial transport and area-varying wave motion on vortex cores, to name only a few examples. Axisymmetric swirling flows are even thought to exhibit such exotic phenomena as finite-time vorticity singularities [1], simulation of which requires extremely high resolution.

This paper presents a Lagrangian vorticity-based method for computation of axisymmetric, viscous fluid flows with or without swirl. Lagrangian vorticity methods are advantageous for simulation of a variety of problems because they are naturally adaptive and they require control points only where significant vorticity exists. Because the control points are transported by the flow, there is no need to discretize the nonlinear advective term, thus avoiding problems with numerical dissipation which plague computational methods utilizing fixed grids [2]. For vortex-dominated flows in particular, Lagrangian vorticity methods have the great advantage of directly evolving the vorticity field which is responsible for generating the flow.

In standard vortex methods, the vorticity field is discretized by a large number of vorticity ''elements,'' which in nonsingular vortex methods are required to overlap, such that the sum of the elements yields a smooth approximation to the desired vorticity field. The vorticity field associated with each element is written as the product of an ''amplitude,'' which is a measure of the total amount of vorticity associated with that element, and a ''weighting function'' or ''core function,'' which specifies how the vorticity is distributed in space. It is typical in vortex methods to solve a transport equation for the element amplitude of a form similar to the inviscid vorticity transport equation. Equivalently, several authors evolve the vorticity via a transport equation, but then set the element amplitude equal to a constant times the vorticity at the element centroid. There is a large literature on inviscid vortex methods for both two- and three-dimensional flows which use this approach, extensive citations to which can be found in the review articles of Leonard [3] and Meiburg [4], including several convergence proofs. For the case of inviscid axisymmetric flows without swirl, a vortex method of this type was employed by Acton [5] to study evolution of large eddies in a jet flow. Strickland and Amos [6] utilized a similar vortex method, but adopted the fast multipole expansion algorithm of Carrier *et al.* [7] to axisymmetric flow without swirl.

An alternative approach, first suggested by Beale [8], is to *fit* the element amplitudes to the vorticity values at the control points, where the vorticity is evolved via the usual transport equation. This amplitude fitting procedure yields essentially a *collocation* approach for solving the Biot–Savart integral. Beale [8] found that the standard vortex method exhibits errors associated with severe distortion of the initial arrangement of control points, which are avoided with use of amplitude fitting. Unfortunately, the system of equations used to fit the element amplitudes is quite large and is also rather ill-conditioned. Beale [8] utilized an iterative procedure to solve this system; however, because the procedure converged to the exact solution of the original ill-conditioned system, the solutions for element amplitude were found to become quite noisy if the system were iterated to convergence. An

approximate iterative procedure was proposed by Marshall and Grant [9], which both converges very quickly and filters out high wavenumber noise due to ill-conditioning of the original system. An error estimate and discussion of filtering properties for this iterative procedure are given in the Appendix of the current paper.

Another challenge for vortex methods lies in development of accurate methods to simulate the viscous diffusion of vorticity. The primary difficulties with accounting for diffusion lie in the problem of accurate calculation of derivatives of a function known only on irregularly spaced control points and in the necessity to adaptively modify the vorticity support to account for the effects of diffusion. A number of differentiation algorithms have been previously proposed in the literature for use with vortex methods [10, 11], but in our experience these methods tend to become increasingly inaccurate as the irregularity in control point spacing increases (see Ref. [12] for a further discussion of this issue). A common device used in simulating boundary layer flows with vortex methods is to interpolate the Lagrangian control points back onto a fixed grid within the boundary layer every few time steps [13, 14], so as to minimize problems with control point irregularity.

A new differentiation method is presented in this paper, which involves fitting a polynomial function to some set of control points surrounding a point at which the derivative is desired and then differentiating the polynomial fit. This differentiation method has been tested by the authors for a variety two- and three-dimensional flows, as well as axisymmetric flows, and has been found to yield highly accurate results which are remarkably insensitive to irregularity of the control points. In the present paper, this differentiation method is employed in conjunction with an extension of the ''diffusion velocity'' scheme of Ogami and Akamatsu [15] and Strickland and Kempka [16], which is used to adaptively move the control points to account for the spreading of the vorticity support due to diffusion.

The Lagrangian vorticity collocation method presented here for axisymmetric flows employs ring-shaped, overlapping elements with Gaussian vorticity variation over the cross section for control points (in the r–z plane) which are located at greater than some specified distance (which is on the order of an element radius) from the symmetry axis. The vorticity at the control points of these ring-shaped elements may have components in the axial, radial, and azimuthal directions. While the azimuthal and radial vorticity must vanish as the distance r from the symmetry axis approaches zero, additional blob-like elements are used to resolve the axial vorticity along the symmetry axis. The induced velocity field is obtained by the Biot–Savart integration over the vorticity field. The vorticity representation is fit to the known vorticity values at the control points at every time step by a collocation procedure which yields a matrix equation for the element amplitudes that is solved using the iterative procedure given in [9].

The computational method is developed for inviscid swirling flows in Section 2, and its extension to viscous flows is presented in Section 3. Validation tests of the method are described for axisymmetric flows without swirl in Section 4, for viscous diffusion in swirling flows in Section 5, and for area-varying wave dynamics on a columnar vortex core in Section 6. Conclusions are given in Section 7.

2. AXISYMMETRIC VORTICITY COLLOCATION METHOD FOR INVISCID FLOWS

The transport equations for the components $(\omega_r, \omega_\theta, \omega_z)$ of vorticity in an axisymmetric inviscid flow, with respect to a cylindrical polar coordinate system (r, θ, z), are given by

$$\frac{d\omega_r}{dt} = \omega_r \frac{\partial u}{\partial r} + \omega_z \frac{\partial u}{\partial z}, \tag{1a}$$

$$\frac{d\omega_\theta}{dt} = \frac{\omega_\theta u}{r} - \frac{2\omega_r v}{r}, \tag{1b}$$

$$\frac{d\omega_z}{dt} = \omega_r \frac{\partial w}{\partial r} + \omega_z \frac{\partial w}{\partial z}, \tag{1c}$$

where d/dt is the material derivative and (u, v, w) are the components of the velocity vector in the radial, azimuthal, and axial directions, respectively. In a domain with no internal or external boundaries, the velocity vector $\mathbf{u}$ can be written as $\nabla \times \boldsymbol{\beta}$, where the vector potential $\boldsymbol{\beta}$ is given by the integral

$$\boldsymbol{\beta}(\mathbf{x}, t) = \frac{1}{4\pi} \int_V \frac{\boldsymbol{\omega}(\mathbf{x}', t)}{s} \, d\nu'. \tag{2}$$

In (2), $d\nu = r \, dr \, dz \, d\theta$ while

$$s = |\mathbf{x} - \mathbf{x}'| = [(z - z')^2 + r^2 + (r')^2 - 2rr' \cos(\theta - \theta')]^{1/2}. \tag{3}$$

The vorticity at field point $\mathbf{x}'$ can be written in terms of the base vectors $(\hat{\mathbf{r}}, \hat{\boldsymbol{\theta}}, \hat{\mathbf{z}})$ at point $\mathbf{x}$ as

$$\begin{aligned} \boldsymbol{\omega}(\mathbf{x}', t) = {} & [\omega_r' \cos(\theta - \theta') + \omega_\theta' \sin(\theta - \theta')]\hat{\mathbf{r}} \\ & + [\omega_\theta' \cos(\theta - \theta') - \omega_r' \sin(\theta - \theta')] \, \hat{\boldsymbol{\theta}} + \omega_z' \hat{\mathbf{z}}, \end{aligned} \tag{4}$$

where $(\omega_r', \omega_\theta', \omega_z')$ are the components of vorticity at $\mathbf{x}'$.

To solve the integral (2) for $\boldsymbol{\beta}$, a representation for the vorticity is used in terms of overlapping vorticity elements of the form

$$\boldsymbol{\omega}(\mathbf{x}, t) = \sum_{n=1}^{N} \mathbf{G}_n(t) f_n(\mathbf{x} - \mathbf{x}_n), \tag{5}$$

where $\mathbf{x}_n$ denote the control point locations (the element centroids in the r–z plane), which are convected by the local fluid velocity:

$$\frac{d\mathbf{x}_n}{dt} = \mathbf{u}(\mathbf{x}_n, t). \tag{6}$$

The elements have the form of rings about the symmetry axis, such that $f_n(\mathbf{x} - \mathbf{x}_n)$ is independent of θ. The element *amplitude* $\mathbf{G}_n$ represents the integral of vorticity associated with the control point over the element cross section. The *weighting function* $f_n(\mathbf{x} - \mathbf{x}_n)$ specifies the distribution of vorticity within the element core and is normalized such that

$$\int_A f_n(\mathbf{x} - \mathbf{x}_n)\, r\, dr\, dz = r_n, \tag{7}$$

where A denotes the r–z plane and r_n is the radial position of control point n. Substituting (5) into (2) and using (4), the contribution $\boldsymbol{\beta}_n$ to the vector potential $\boldsymbol{\beta}$ from element n can be written as

$$\boldsymbol{\beta}_n = \frac{\hat{\mathbf{r}}}{4\pi}[G_r I_1 + G_\theta I_2] + \frac{\hat{\boldsymbol{\theta}}}{4\pi}[G_\theta I_1 - G_r I_2] + \frac{\hat{\mathbf{z}}}{4\pi} G_z I_3, \tag{8}$$

where

$$I_1 = \int_V \frac{\cos(\theta - \theta')}{s} f_n(\mathbf{x}' - \mathbf{x}_n)\, d\nu', \tag{9a}$$

$$I_2 = \int_V \frac{\sin(\theta - \theta')}{s} f_n(\mathbf{x}' - \mathbf{x}_n)\, d\nu', \tag{9b}$$

$$I_3 = \int_V \frac{f_n(\mathbf{x}' - \mathbf{x}_n)}{s}\, d\nu', \tag{9c}$$

and (G_r, G_θ, G_z) are components of $\mathbf{G}_n$.

Letting the weighting function $f_n(\mathbf{x} - \mathbf{x}_n)$ approach a constant times a Dirac delta and using standard integral formulas [17] to solve (9a)–(9c), we obtain

$$\boldsymbol{\beta}_n = \frac{1}{2\pi}\left(\frac{r_n}{r}\right)^{1/2} (G_r \hat{\mathbf{r}} + G_\theta \hat{\boldsymbol{\theta}}) \left[\left(\frac{2}{k_n} - k_n\right) K(k_n) - \frac{2}{k_n} E(k_n)\right] + \frac{1}{2\pi}\left(\frac{r_n}{r}\right)^{1/2} G_z k_n K(k_n) \hat{\mathbf{z}}, \tag{10}$$

where

$$k_n^2 \equiv \frac{4 r r_n}{(z - z_n)^2 + (r + r_n)^2} \tag{11}$$

and $K(\cdot)$ and $E(\cdot)$ are complete elliptic integrals. Taking the curl of (10), the velocity contribution $\mathbf{u}_n$ from element n, with components (u_n, v_n, w_n), is given by

$$u_n(r,\theta,z,t) = \frac{(z-z_n)G_\theta k_n}{4\pi(r_n r^3)^{1/2}k_n'^2}\left[\left(1-\frac{1}{2}k_n^2\right)E(k_n) - k_n'^2 K(k_n)\right], \tag{12a}$$

$$v_n(r,\theta,z,t) = -\frac{(z-z_n)G_r k_n}{4\pi(r_n r^3)^{1/2}k_n'^2}\left[\left(1-\frac{1}{2}k_n^2\right)E(k_n) - k_n'^2 K(k_n)\right]$$
$$-\frac{r_n G_z k_n}{4\pi(r_n r^3)^{1/2}k_n'^2}\left[-k_n'^2 K(k_n) + \left\{1-\frac{1}{2}k_n^2\left(1+\frac{r}{r_n}\right)\right\}E(k_n)\right], \tag{12b}$$

$$w_n(r,\theta,z,t) = \frac{k_n G_\theta}{8\pi(r_n r^3)^{1/2}k_n'^2}[(r+r_n)k_n^2 E(k_n) - 2r\{E(k_n) - k_n'^2 K(k_n)\}], \tag{12c}$$

where $k_n'^2 \equiv 1 - k_n^2$. It is noted that u_n and w_n depend only on G_θ and are the same as the Helmholtz solution for the velocity induced by a vortex ring of circulation G_θ. The only effect of the radial and axial vorticity components is on the swirling component, v_n, of the velocity. For optimal code performance, the elliptic integrals $K(\cdot)$ and $E(\cdot)$ in (12) are precomputed over a uniform one-dimensional grid and then obtained during the flow calculation using a lookup and interpolation procedure.

The velocity expressions (12) become singular as the field point $\mathbf{x}$ approaches the element centroid $\mathbf{x}_n$. Element singularities are typically regularized in two- and three-dimensional vortex blob methods by using nonsingular expressions for the weighting function $f_n(\mathbf{x}-\mathbf{x}_n)$, such as the Gaussian

$$f_n(\mathbf{x}-\mathbf{x}_n) = C_n \exp\left[-\frac{(z-z_n)^2+(r-r_n)^2}{\delta_n^2}\right], \tag{13}$$

where δ_n is the element "radius." The constant C_n is determined from the normalization condition (6) as

$$C_n = \frac{2r_n}{\pi^{1/2}\delta_n^3 + 2\pi r_n \delta_n^2}. \tag{14}$$

In an axisymmetric flow, where each element forms a ring about the symmetry axis, the integrals (8) are very hard to evaluate exactly for nonsingular weighting functions. We instead employ an approximate procedure which assumes that the ratio δ_n/r_n of the element radius to the radial position of the element contol point is small. For Gaussian elements, the integrals (8) reduce to Laplace integrals which can be evaluated with standard asymptotic methods [18]. The resulting regularized velocity expressions are given simply by multiplying (12) by the regularizing function

$$\xi(\mathbf{x}-\mathbf{x}_n) = 1 - \exp\left[-\frac{(z-z_n)^2+(r-r_n)^2}{\delta_n^2}\right]. \tag{15}$$

The self-induced velocity, $\mathbf{w}_n$, of a ring-like element has the form [19]

$$\mathbf{w}_n = \frac{G_\theta}{4\pi r_n}\left[\ln\left(\frac{8r_n}{\delta_n}\right) + C\right]\hat{\mathbf{z}}, \tag{16}$$

where C is an order unity constant that depends on the vorticity profile within the element cross section. The importance of the self-induced velocity, in comparison with the velocity induced by all of the other vorticity elements, depends on the resolution of the flow field. For instance, if an isolated vortex ring, of ring radius R, core radius σ, and strength Γ, is formed of N ring-like vorticity elements of equal strength, the amplitude of each element will be given by $\mathbf{G}_n = (\Gamma/N)\hat{\boldsymbol{\theta}}$. Assuming that the element radii δ_n are fit to maintain a prescribed overlap of the fluid elements, then $\delta_n \cong B(\pi\sigma^2/N)^{1/2}$, where B is a constant of order unity. Taking $r_n \cong R$ for a thin-core vortex ring, the ratio of the self-induced velocity of the vorticity elements to the propagation velocity of the ring as a whole has the form $[\ln(\sqrt{N}) + E]/NF$, where E and F are constants of order unity. Since the logarithmic terms change very slowly with N, we find that the self-induced velocity contributes an amount of order approximately $1/N$ of the total self-induced velocity of the ring. Some computations showing the effect of the self-induced velocity are given by Strickland and Amos [6], who concluded that for a well-resolved vorticity field, the element self-induced velocity is negligible.

The regularization (15) has been tested using a variety of validation calculations (see Section 5) and is found to perform well even in cases where $\delta_n = O(r_n)$. However, very close to the symmetry axis the thin-core assumption must clearly break down, especially since the algorithm used to fit the element amplitudes (to be stated presently) requires the elements to overlap sufficiently. To overcome this difficulty, ring-type elements are excluded from a thin cylindrical region of radius R_E about the symmetry axis. To account for the nonzero axial vorticity that may be present on the symmetry axis itself, a different blob-type element is introduced whose centroid lies directly on the symmetry axis. We use a Gaussian form for the blob-type elements of the same form as given in (13). The normalization for blob-like elements is given by an expression similar to (6) with r_n replaced by the "exclusion radius" R_E on the right-hand side, which yields an expression for the normalization constant for blob-like elements of the form

$$C_n = \frac{2R_E}{\pi^{1/2}\delta_n^3}. \tag{17}$$

The velocity induced by a blob-like element n at field point $\mathbf{x}$ has the form [9]

$$\mathbf{u}_n(\mathbf{x}, t) = \frac{P\left(\frac{3}{2}, \frac{|\mathbf{x} - \mathbf{x}_n|^2}{R_n^2}\right)\delta_n^3\pi^{1/2}\, C_n}{4|\mathbf{x} - \mathbf{x}_n|^3}\mathbf{G}_n \times (\mathbf{x} - \mathbf{x}_n), \tag{18}$$

where $P(a, z)$ is the incomplete gamma function, with limits $P = 0$ at $z = 0$ and $P = 1$ as $z \to \infty$. When $a = 3/2$ and $z = x^2$, for some real variable x, a convenient expression for $P(3/2, x^2)$ is given in terms of the error function $\mathrm{erf}(x)$ as [20]

$$P\left(\frac{3}{2}, x^2\right) = \mathrm{erf}(x) - \frac{2xe^{-x^2}}{\sqrt{\pi}}. \tag{19}$$

The element amplitudes are obtained by fitting the vorticity representation (5) to the known vorticity values at the control points (obtained by solution of (1)) at every time step. Evaluating the representation (5) at the element control points gives an $N \times N$ matrix equation for the amplitudes $\mathbf{G}_n$ of the form

$$\boldsymbol{\omega}_m = \sum_{n=1}^{N} \mathbf{G}_n(t)\, W_{mn}, \tag{20}$$

where $\boldsymbol{\omega}_m = \boldsymbol{\omega}(\mathbf{x}_m)$ and $W_{mn} \equiv f_n(\mathbf{x}_m - \mathbf{x}_n)$. However, for overlapping elements, the matrix equation (20) is ill-conditioned, as noted for two-dimensional vortex blob methods by Beale [8], such that use of the exact solution of (20) for $\mathbf{G}_n$ in (5) yields a very noisy vorticity representation, even when the actual vorticity field is quite smooth. The difficulties in solving (20) are similar to those which arise, for instance, in discretization of Fredholm integral equations of the first kind [21].

An approximate iterative procedure was introduced by Marshall and Grant [9] for solution of (20), in which $\mathbf{G}_n$ is determined by

$$\boldsymbol{\omega}(\mathbf{x}_m, t) = \mathbf{G}_m^{(q+1)} \sum_{n \in Q(m)} W_{mn} + \sum_{n \in P(m)} W_{mn} \mathbf{G}_n^{(q)}. \tag{21}$$

In this procedure, the amplitude is *temporarily* assumed to be constant over a set of points $Q(m)$ sufficiently close to the given point m. The set $P(m)$ is the complement of $Q(m)$, and q is an iteration index. This iterative procedure both speeds up the matrix inversion to an $O(N)$ process and smooths out the vorticity representation. The procedure (21) is typically found to converge very quickly to a maximum relative error of less than 10^{-6} (within about 5–10 iterations), and the number of iterations required for convergence seems to be independent of the number of control points. This procedure can be used to simultaneously obtain the amplitudes of both the off-center ring-like elements and the center blob-like elements, since both types of elements are normalized in a similar way. Validation tests for this iterative procedure are given in Ref. [9], and derivation of error and smoothing properties of the iteration is discussed in the Appendix.

One advantage of the amplitude-fitting procedure (21) is that it is very simple to eliminate or add new control points while maintaining a smooth vorticity field. For instance, in the viscous flow calculations to be discussed in the next section, it is desirable to combine control points which come too close to each other, in order that the diffusion computation remains stable for a given time step. Combining two control points, labeled 1 and 2, is performed by adding a new control point at the centroid of points 1 and 2, where the vorticity at the new point is the average of the vorticity at points 1 and 2, and then eliminating points 1 and 2. When a control point of a ring-like element enters into the exclusion region with radius R_E surrounding the symmetry axis, the point is eliminated and a new point is added at the reflected location of the original point. The vorticity at this new point is obtained by interpolation using the blob representation (5). Because the element amplitudes are continually refit to the vorticity values at the control points, the process of adding and eliminating control points is simply a matter of changing resolution and

does not result in a net vorticity loss or supplement to the flow field (aside from fluctuations associated with discretization errors).

3. ALGORITHM FOR VISCOUS DIFFUSION

In order to account for viscous diffusion of vorticity in the context of a Lagrangian method, it is necessary to implement some algorithm which can both (1) modify the vorticity support to continuously cover the vorticity field with elements during the diffusion process and (2) calculate derivatives of various quantities whose values are known only on irregularly spaced points. Many early vortex methods simulated viscous diffusion by adding a random walk to the element positions [22], which both adaptively spreads the vorticity support and avoids the differentiation problem. However, random walk is quite noisy, as demonstrated by Ghoniem and Sherman [23], and it is not consistent with the procedure (21) used to fit element amplitudes.

(a) *Modification of Vorticity Support*

In the current paper, the vorticity support is modified adaptively by a three-dimensional extension of the *diffusion velocity* scheme (originally proposed by Ogami and Akamatsu [15] and corrected by Kempka and Strickland [16] for two-dimensional flows). With this scheme, the control points are advected by the sum of the local material velocity $\mathbf{u}$ and some vector $\mathbf{v}$, called the diffusion velocity, which accounts for the effect of diffusion on the vorticity support. The expression for diffusion velocity typically used for two-dimensional flows, as proposed by Ogami and Akamatsu [15], is

$$\mathbf{v} \equiv -\frac{\nu}{\omega}\nabla\omega = -\nu\nabla(\ln\omega). \tag{22}$$

The expression in terms of the logarithm in (22) is preferable, since both ω and its gradient may be small near the outer regions of the vorticity field without $\mathbf{v}$ being small. The expression (22) for $\mathbf{v}$ can be interpreted simply as the vorticity flux divided by the vorticity magnitude. If C is a closed circuit bounding an open surface A, which are advected by the sum $\mathbf{u} + \mathbf{v}$ of the material and diffusion velocities, then the integral of the vorticity over A is invariant in time in a two-dimensional flow.

In a three-dimensional flow, sufficient condition for the integral of vorticity normal to a convected open surface A to be invariant is that the diffusion velocity satisfy the equation [16]

$$\mathbf{v} \times \boldsymbol{\omega} + \nu\nabla \times \boldsymbol{\omega} = 0. \tag{23}$$

A solution of Eq. (23) exists if and only if the vorticity vector $\boldsymbol{\omega}$ is complex-lamellar, such that $\boldsymbol{\omega} \cdot (\nabla \times \boldsymbol{\omega}) = 0$. While this condition may be satisfied in some special cases, such as two-dimensional flow or axisymmetric flow without swirl, it does not hold for general three-dimensional flows.

The purpose of the diffusion velocity is to maintain coverage of the vorticity support by the control points throughout the computation. In the current work, we assume a locally two-dimensional diffusion process and ignore the diffusion velocity in the direction of the vortex lines. It is noted that if the vorticity field is adequately resolved at any given time, then there will already exist control points all along vortex lines. While we hope that further research will bring improved expressions for the diffusion velocity in three-dimensional flows, for the time being the expression (22) seems to be adequate for our purposes and will be used in the remainder of the paper.

The rate of change of vorticity at a specified control point is not given by the material derivative, $d\boldsymbol{\omega}/dt$, since the control points are not advected as material points, but instead by a different derivative, $d_v\boldsymbol{\omega}/dt$, defined by

$$\frac{d_v\boldsymbol{\omega}}{dt} \equiv \frac{\partial \boldsymbol{\omega}}{\partial t} + [(\mathbf{u} + \mathbf{v}) \cdot \boldsymbol{\nabla}]\boldsymbol{\omega} = \frac{d\boldsymbol{\omega}}{dt} + (\mathbf{v} \cdot \boldsymbol{\nabla})\boldsymbol{\omega}. \tag{24}$$

Adding $(\mathbf{v} \cdot \boldsymbol{\nabla})\boldsymbol{\omega}$ to both sides of the vorticity transport equation for a viscous flow, the equation governing the rate of change of vorticity at a control point is given by

$$\frac{d_v\boldsymbol{\omega}}{dt} = (\boldsymbol{\omega} \cdot \boldsymbol{\nabla})\mathbf{u} + \nu\nabla^2\boldsymbol{\omega} + (\mathbf{v} \cdot \boldsymbol{\nabla})\boldsymbol{\omega}. \tag{25}$$

Writing the vorticity vector as the product of its magnitude ω and a unit direction $\mathbf{a}$ and denoting the sum of the last two terms in (25) by the vector $\mathbf{D}$, we can use (22) to write

$$\mathbf{D} = \nu\omega\,\nabla^2(\ln \omega)\mathbf{a} - \omega(\mathbf{v} \cdot \boldsymbol{\nabla})\mathbf{a} + \nu\omega\,\nabla^2\mathbf{a}. \tag{26}$$

In order to obtain $\mathbf{v}$ and the diffusion term $\mathbf{D}$, it is necessary to approximate the first and second derivatives of $\ln \omega$ and two components of the vector $\mathbf{a}$. Derivatives of the third component of $\mathbf{a}$ can be obtained from the derivatives of the first two components and the observation that $\mathbf{a}$ is a unit vector.

The results (22)–(26) hold for all three-dimensional flows, and simplifications for axisymmetric flows are obtained simply by writing (22)–(26) in cylindrical polar coordinates and dropping all derivatives with respect to θ. For control points located on the symmetry axis, only the axial components of $\mathbf{v}$ and $\mathbf{D}$ are nonzero. Since the vorticity flux (and hence the radial vorticity gradient) must vanish as $r \to 0$, a Taylor series expansion of $\ln \omega$ about the symmetry axis gives

$$\ln \omega(r, z, t) = \ln \omega(0, z, t) + \frac{r^2}{2}\left.\frac{\partial^2(\ln \omega)}{\partial r^2}\right|_{r=0} + O(r^3). \tag{27}$$

Differentiating (27) with respect to r, dividing by r, and then taking the limit as $r \to 0$ yields

$$\lim_{r\to 0} \frac{1}{r}\frac{\partial(\ln \omega)}{\partial r} = \left.\frac{\partial^2(\ln \omega)}{\partial r^2}\right|_{r=0}. \tag{28}$$

An equation similar to (28) can also be written for the radial derivative of the axial component of the vector **a**.

(b) *Differentiation on Irregularly Spaced Points*

In the present paper, derivatives are computed using a *moving least-square* method, in which a polynomial is fit to the values of some function $T(x)$, in the region about each point x_m, where the derivatives of $T(x)$ are desired, by minimizing a localized least-square error. For instance, in one dimension a quadratic approximation $q_m(t)$ to $T(x)$, in the neighborhood of the point x_m, has the form

$$q_m(x) \equiv T_m + B_m\left(\frac{x - x_m}{\delta}\right) + C_m\left(\frac{x - x_m}{\delta}\right)^2, \tag{29}$$

where $T_m \equiv T(x_m)$ and B_m and C_m are unknown coefficients. An "error" J_m is defined by

$$J_m \equiv \sum_{n=1}^{N} L_{nm}[T_n - q_m(x_n)]^2, \tag{30}$$

where L_{nm} is a localizing function. A convenient choice for L_{nm} is

$$L_{nm} = \exp\left[-\frac{(x_n - x_m)^2}{\delta^2}\right], \tag{31}$$

where δ is a length scale of $O(\Delta x)$. The error is minimized by setting the partial derivatives of J_m with respect to B_m and C_m equal to zero, yielding a system of two linear algebraic equations for these coefficients of the form

$$\frac{\partial J_m}{\partial B_m} = 0 = \sum_{n=1}^{N} L_{nm}[T_n - q_m(x_n)]\left(\frac{x_n - x_m}{\delta}\right) \tag{32a}$$

$$\frac{\partial J_m}{\partial C_m} = 0 = \sum_{n=1}^{N} L_{nm}[T_n - q_m(x_n)]\left(\frac{x_n - x_m}{\delta}\right)^2. \tag{32b}$$

Once B_m and C_m are obtained by solution of (32a) and (32b), the first and second derivatives of $T(x)$ at x_m are given simply by B_m/δ and $2C_m/\delta^2$, respectively.

Tests of this differentiation algorithm were performed in one dimension using the Gaussian function $T(x) = \exp(-x^2)$. In these tests, the control points are initially distributed over an interval $(-3, 3)$ with uniform spacing Δx, and they are then randomly displaced with an amplitude $\varepsilon\Delta x$, where ε is a measure of control point irregularity. A plot of the second derivatives of T computed by solution of the

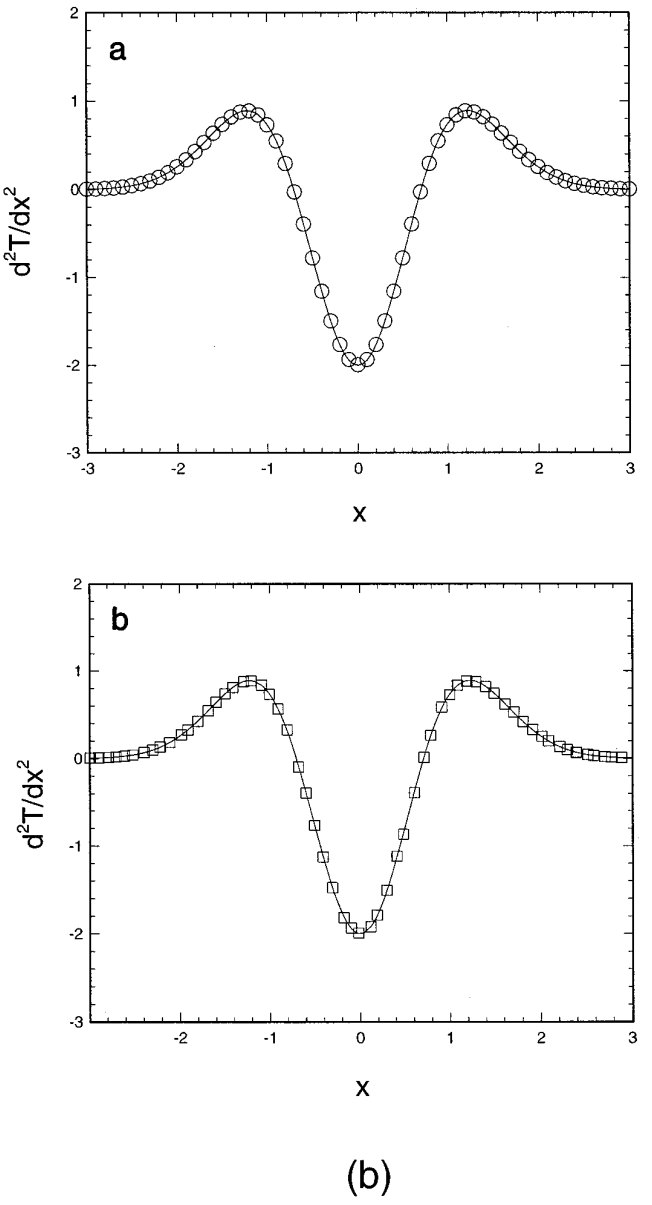

FIG. 1. Plot of the second derivatives of a Gaussian function $T = \exp(-x^2)$ in one dimension as computed using the moving least-square method for (a) $\varepsilon = 0$ (circles) and (b) $\varepsilon = 0.4$ (squares), in comparison to the exact result (solid curve). The average control point spacing is $\Delta x = 0.05$ and the localization length scale is $\delta = 2\Delta x$.

system (32), with $\delta = 2\Delta x$ and $\Delta x = 0.05$, is given in Fig. 1 for a case with a uniform grid (circles) and a case of very irregular point spacing with $\varepsilon = 0.4$ (squares), in comparison to the exact second derivative shown by a solid curve. The relative root-mean-square (*rms*) error, defined as the root-mean-square error divided by the maximum value of the second derivative over the computed interval, is plotted

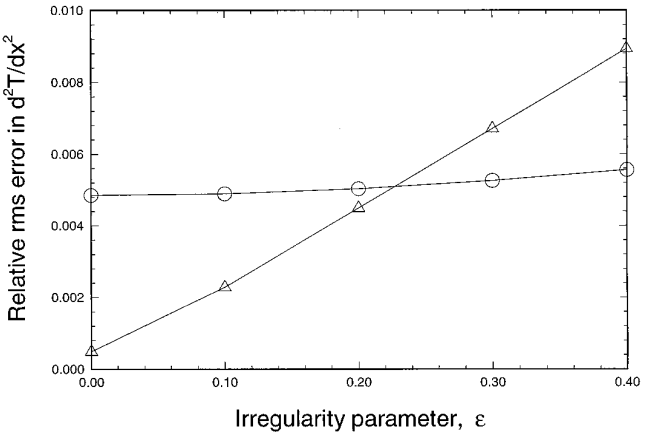

FIG. 2. Plot showing the variation of the relative root-mean-square error as a function of the irregularity parameter ε for the one-dimensional test described in the caption to Fig. 1, both for the moving least-square method (circles) and for the standard centered-difference method for irregularly spaced points (triangles).

in Fig. 2 as a function of ε both for the moving least-square method (circles) and for the standard centered-difference approximation for irregularly spaced points (triangles). The *rms* error for the moving least-squares method is remarkably insensitive to change in ε.

The convergence rate of the moving least-square method was examined by performing runs with different values of Δx for both $\varepsilon = 0$ and $\varepsilon = 0.4$. The results, shown on a log–log scale in Fig. 3, indicate a convergence rate of about 1.9 both for the case of a uniform grid ($\varepsilon = 0$) and for the case with very irregularly spaced points ($\varepsilon = 0.4$). By contrast, the convergence rate of the second derivative for

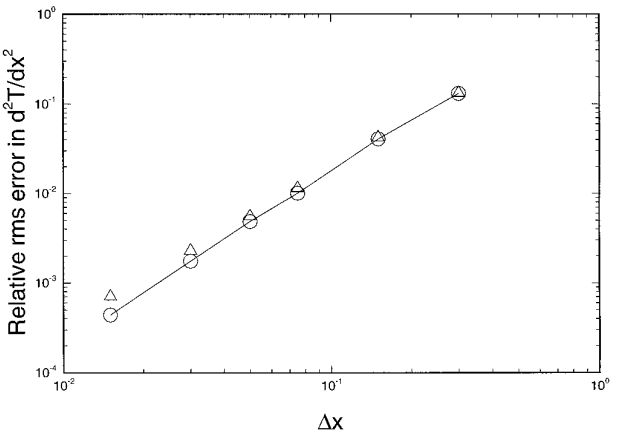

FIG. 3. Log–log plot showing the convergence rate of the moving least-square method for the one-dimensional test described in the caption of Fig. 1, with $\varepsilon = 0$ (circles) and $\varepsilon = 0.4$ (triangles). The slope of the best-fit line for the $\varepsilon = 0$ case is approximately 1.9.

the standard centered-difference approximation on a randomly perturbed grid is approximately first-order in Δx [24].

Tests have also been performed with various values of the length scale δ (see [12]). It is found that the predictions of the moving least-square method are not particularly sensitive to this parameter for $\delta > \Delta x$, although the best results are obtained for δ between about 1 and 3 times Δx. For values of δ much less than Δx, the error from the moving least-squares method increases for irregularly spaced points as δ is decreased, whereas for uniformly spaced points the moving least-square method reduces to the standard centered-difference approximation as $\delta \to 0$.

In the solution of the vorticity transport equations of the form (25), differentiation of $\ln \omega$ and of the components of the unit vector **a** is necessary in order to obtain the vectors **v** and **D** in (22) and (26). Furthermore, differentiation of the radial and axial velocity components is necessary in order to obtain the vortex stretching terms in (1). In an axisymmetric flow, the first and second derivatives of some function $f(r, z)$ at a point (r_m, z_m) are approximated by differentiating a polynomial fit of the form

$$q_m(r, z) \equiv f_m + \left(\frac{r - r_m}{\delta_m}\right) + C_m\left(\frac{z - z_m}{\delta_m}\right) + D_m\left(\frac{r - r_m}{\delta_m}\right)\left(\frac{z - z_m}{\delta_m}\right) + E_m\left(\frac{r - r_m}{\delta_m}\right)^2 + F_m\left(\frac{z - z_m}{\delta_m}\right)^2. \tag{33}$$

An "error" J_m is defined by

$$J_m \equiv \sum_{n=1}^{N} L_{mn}[f_n - q_m(r_n, z_n)]^2, \tag{34}$$

where we choose

$$L_{nm} = \exp\left[-\frac{(r_n - r_m)^2 + (z_n - z_m)^2}{\delta_m^2}\right]. \tag{35}$$

Minimizing J_m with respect to the coefficients in (33) yields

$$\sum_{n=1}^{N} L_{nm}\left(\frac{r_n - r_m}{\delta_m}\right)^i\left(\frac{z_n - z_m}{\delta_m}\right)^j [f_n - q_m(r_n, z_n)] = 0,$$
$$\{i, j: (i, j) \in (0, 1, 2); 0 < i + j < 3\}. \tag{36}$$

Equation (36) represents a system of five linear equations for the five unknown coefficients in (33). After solution for these coefficients, the gradient and Laplacian of $f(r, z)$ are approximated by

$$\nabla f|_m \cong \frac{1}{\delta_m}(B_m \mathbf{e}_r + C_m \mathbf{e}_z), \tag{37a}$$

$$\nabla^2 f|_m \cong 2\frac{E_m + F_m}{\delta_m^2}. \tag{37b}$$

4. VALIDATION TESTS FOR AXISYMMETRIC FLOWS

The axisymmetric vorticity collocation method was tested using a variety of validation calculations, in which the evolution of the computed flow over time is compared to different analytical results. The first two test calculations, reported in this section, involve inviscid axisymmetric flows without swirl.

The first set of test calculations examines the ability of the axisymmetric vortex method to replicate the self-induced velocity of thin-core vortex rings. Test calculations were performed using 316 vorticity elements initially distributed within a torus of circular cross-section, which formed a vortex ring of strength Γ, nominal core radius σ, and ring radius R. In the following, all length, time, and velocity scales are nondimensionalized by σ, σ^2/Γ, and σ/Γ, respectively. The radii δ_n of the vorticity elements was set adaptively to be approximately twice the distance to the nearest element control points and had a mean value of about 0.2. The vorticity at the control point locations was initially prescribed to be proportional to the radial distance r from the symmetry axis. Calculations were performed with different values of R, in each of which the distance of ring centroid propagation was measured over a fixed time interval $0 \leq t \leq 50$. Each computation lasted for 500 time steps, and the rings were observed to propagate over a distance of between 2 to 4.5 core radii. The vorticity contours were nearly constant with time during all runs, aside from some slight deformation of the core shape for small values of R.

While the outermost element controids were placed at a distance equal to the nominal core radius from the center axis of the ring, the vorticity distribution within the ring cross section had a larger effective radius σ_E, given approximately by the sum $\sigma + \overline{\delta}$ of the nominal core radius and the average blob radius, due to the fact that vorticity associated with the outermost blobs decayed exponentially outside of the nominal core radius with a typical length scale $\overline{\delta}$. A plot comparing the computed ring propagation speeds versus the theoretical value for uniform vorticity distribution [25], given by

$$U \cong \frac{1}{4\pi R}\left[\ln(8R/\sigma_E) - 0.25\right], \tag{38}$$

is shown in Fig. 4, where the theoretical results for effective (dimensionless) radius $\sigma_E = 1 + \overline{\delta} \cong 1.2$ are shown by a solid curve. The theoretical results agree well with the computed results, with a difference less than 1.0% for $R \geq 4$. The computed results deviate somewhat more from the predictions of (38) for $R \leq 3$, as would be expected from the observation that the thin-core ring theory used to obtain (38) breaks down for small R.

The second test calculation examines the evolution of the spherical vortex of Hill [26]. This calculation was performed using 1900 ring-like vorticity elements, whose centroids were initially randomly distributed in a half circle of radius a centered at the origin of the cylindrical coordinate system, and 100 blob-like elements with control points placed directly on the symmetry axis. The vorticity field is proportional to the radial distance r from the symmetry axis, and the vortex strength is denoted by A. For this test, length, time, and velocity scales are nondimen-

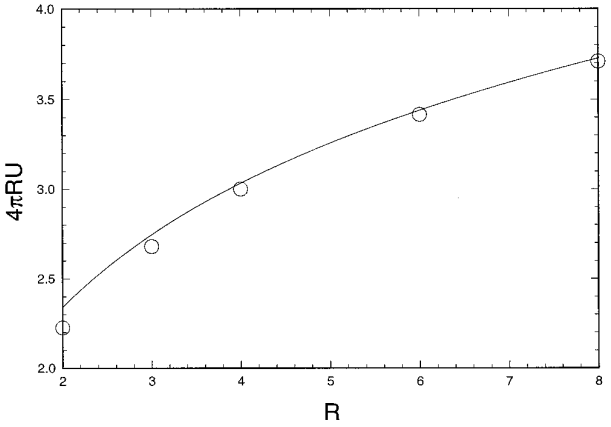

FIG. 4. Plot of dimensionless self-induced ring propagation speed as a function of dimensionless ring radius. The theoretical prediction from Eq. (38) with effective radius $\sigma_E = 1.2$ is indicated by a solid curve and the computational results are indicated by circles.

sionalized by a, $1/(aA)$, and a^2A, respectively. The mean value of the element radius δ_n was about 0.09 during the calculation, so that the effective radius of the spherical vortex was $a_E = 1 + \overline{\delta} \cong 1.09$. The solution of Hill [26] gives the dimensionless propagation speed of the vortex as

$$U = \frac{2}{15} a_E^2. \tag{39}$$

The computation examined the vortex evolution over a time interval $0 \leq t \leq 30$, which was discretized using 300 equal time steps. Computational results are shown in Fig. 5 at two time steps. During the computation, the vortex propagated a distance of nearly five sphere radii. The computed propagation speed of the vortex centroid during this time interval was 0.157 ± 0.003, while the theoretical propagation speed based on (39) was 0.158. The vorticity magnitude remained proportional to the radial distance r from the symmetry axis throughout the run. It is noted that the spherical vortex is unstable to axisymmetric disturbances [27], which leads to shedding of vorticity elements in a tail behind the vortex during the later parts of the

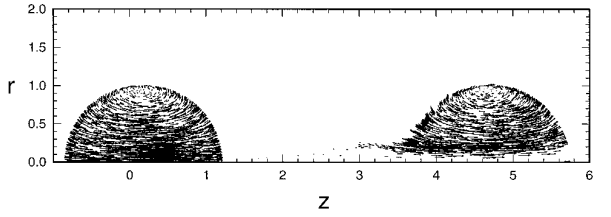

FIG. 5. Velocity vectors, attached to each control point, for a simulation of Hill's spherical vortex. The vectors are plotted at times $t = 0.9$, just after initiation, and $t = 29.9$. A trailing "tail" is apparent at the later time due to vortex instability.

computation (see Fig. 5). As noted previously by Pozrikidis [28], the vorticity nearest the axis of symmetry is swept downstream and the spherical vortex evolves into a fat-cored vortex ring of the class considered by Norbury [29].

5. VALIDATION TESTS FOR THE VISCOUS DIFFUSION METHOD

Validation tests are presented in this section for the moving least-square viscous diffusion method in an axisymmetric swirling flow. We examine the diffusion of a columnar vortex, centered on the symmetry axis, with Gaussian distributions of both axial velocity and axial vorticity. The flow is assumed to be periodic over a length L in the direction of the symmetry axis. The periodic boundary condition was enforced by including one period of the vorticity field in the Biot–Savart integral on each side of the computed section of the flow. The calculation was initiated by placing points on a uniform grid in the region $-L/2 < z < L/2$ and $0 < r < a$ of the r–z plane, where the bottom row of points on this grid were placed on the symmetry axis. The points off the symmetry axis were then randomly displaced by an amount with maximum value of 30% of their initial separation distance, so that the initial point spacing was quite irregular. The axial vorticity distribution was initially prescribed to be proportional to the Gaussian $\exp(-r^2/\sigma^2)$ with "radius" σ, and the azimuthal vorticity distribution was initially proportional to the product of the radial distance r times a Gaussian of radius σ. The magnitudes of the axial and azimuthal vorticity were scaled to yield a prescribed vortex circulation Γ and axial flow rate Q on the initial plane. In the remainder of this section, all length, time, and velocity variables are nondimensionalized by a, a^2/Γ, and a/Γ, respectively. In the computations, the period length $L = 4$ and the Gaussian radius $\sigma = 0.5$.

The diffusion was performed using an explicit second-order predictor–corrector method for which the stability condition has the form

$$\Delta t \le \frac{s\ell^2}{2\nu}, \tag{40}$$

where ℓ is the minimum distance between any two control points, ν is the kinematic viscosity, and s is an adjustable constant. In numerous tests, for both two-dimensional and axisymmetric flow, we have found that the moving least-square diffusion scheme is stable provided that s is less than about 5–7. The time step was set adaptively according to (40), where in the present computations we set $s = 0.5$. A minimum value of the separation distance ℓ was prescribed, such that when two control points approached closer than this minimum distance they were combined using the procedure described in Section 2.

Analytical solutions for variation of the axial and azimuthal vorticity and velocity components are given by

$$\begin{aligned} \omega_z &= \frac{\Gamma}{\pi R^2}\exp(-r^2/R^2), \quad \omega_\theta = \frac{2Qr}{\pi R^4}\exp(-r^2/R^2), \\ u_z &= \frac{Q}{\pi R^2}\exp(-r^2/R^2), \quad u_\theta = \frac{\Gamma}{2\pi r}[1-\exp(-r^2/R^2)], \end{aligned} \tag{41}$$

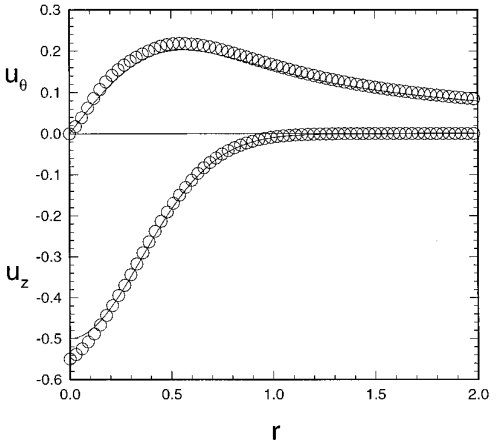

FIG. 6. Plot of the computed axial and azimuthal velocity profiles (circles) versus the theoretical values (solid curves) for a columnar vortex with prescribed Gaussian axial vorticity profile and Gaussian axial velocity profile.

where $R(t) \equiv 4\nu(t + t_0)$. A comparison of the computed and analytical induced axial and azimuthal velocity components at the initial time is shown in Fig. 6, which was obtained for a case initiated with 21 points in the radial direction and 51 points in the axial direction (or 1071 total points) prior to the random displacement. The computed velocities compare well with the analytical expressions, with the exception of a slight offshoot of the axial velocity near the symmetry axis, which occurs due to breakdown of the assumption that δ_n/r_n is small. This offshoot can be further reduced by increasing the resolution of control points near the symmetry axis, thereby decreasing the element radius δ_n.

Computations were performed to assess the accuracy of the vorticity diffusion algorithm for this flow for a case with vortex Reynolds number, $\mathrm{Re} = \Gamma/\nu$, equal to 10. The effect of resolution on the accuracy of the diffusion computations was assessed by varying the number, N_r, of elements spanning the vortex over a radial distance of 2σ. Test computations were performed with $N_r = 21$, 11, and 5 for which the number of elements spanning the axial length L of one period of the vortex was set to 51, 35, and 15, respectively. The element radius δ_n was fit adaptively at each time step to be about twice the distance between a control point and its closest few neighboring control points. The control point locations move outward under the diffusion velocity for this flow, such that the furthest control points traveled from an initial radius of 1.0 to a radius of about 2.6 during the course of the computations. The variation of the axial and azimuthal vorticity components with radial distance is shown in Fig. 7 for a case with $N_r = 21$ at five different times. In this plot, the computed results are indicated by symbols and the theoretical values from (41) are indicated by solid curves. The vorticity magnitude decreases by a little over an order of magnitude during this run, but the computed results are found to remain extremely close to the analytical solution

The maximum error in the computational results was found to be about 1.6%, 7.5%, and 11% of the analytical solution for cases with $N_r = 21$, 11, and 5, respectively.

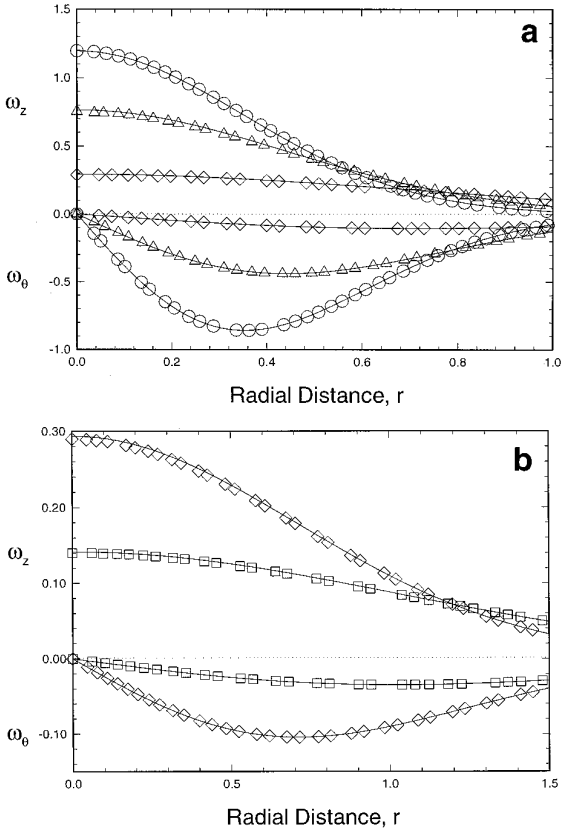

FIG. 7. Comparison of the computed (symbols) and theoretical (solid curves) axial and azimuthal vorticity profiles for a diffusing vortex core. The initial axial vorticity and axial velocity profiles are proportional to a Gaussian with radius 0.5, and the vortex Reynolds number $\mathrm{Re} \equiv \Gamma/\nu = 10$. The profiles are shown in (a) at times $t = 0$ (circles), 0.659 (triangles), and 1.48 (diamonds) and in (b) at times $t = 1.48$ (diamonds) and 4.66 (squares) for a case with initially $N_r = 21$ control points in the radial direction and 51 control points in the axial direction.

Moreover, the percentage error does not increase monotonically in time, but rather is observed to decrease near the end of the computation. The computational results for the maximum axial vorticity component are plotted against the analytical prediction from (46) in Fig. 8 for cases with the three different values of radial resolution N_r. Other test calculations have been performed using a similar diffusion method for two-dimensional Gaussian vortex patches and are found to continue to yield excellent agreement with the analytical solution for extremely long time intervals, during which the vorticity magnitude was reduced by over two orders of magnitude.

6. VALIDATION TESTS FOR VORTEX WAVE DYNAMICS

The final validation test examines unforced oscillation of a columnar vortex due to variation in core radius. In the test computations, the core radius is initiated as a cosine wave with mean value σ_0 and wavelength $4\sigma_0$. The core is discretized by

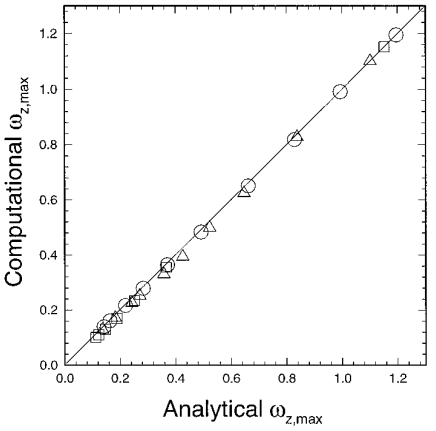

FIG. 8. Plot of maximum axial vorticity component, at various times, as determined by computations versus analytical values, for diffusion of a columnar Gaussian vortex with axial flow at a vortex Reynolds number of 10. Results for $N_r = 21$ are denoted by circles; results for $N_r = 11$ are denoted by triangles; and results for $N_r = 5$ are denoted by squares.

1619 ring-like vorticity elements for off-center points and 81 blob-like elements are placed along the symmetry axis. The axial component of the initial vorticity field is specified to be independent of r and to vary with z in such a way that the circulation remains constant along the vortex axis. The radial component of the initial vorticity is specified to vary linearly with r, such that the vorticity vector is parallel to the core boundary for the outermost points on the vortex core. One period on each side of the computed section is used in the velocity calculation.

Models for evolution of the axial velocity $w(z, t)$ and core radius $\sigma(z, t)$ of a columnar vortex were developed using a variety of different approaches by Lundgren and Ashurst [30], Marshall [31], and Leonard [32], all of which yield essentially the same one-dimensional wave equations for long, weakly nonlinear area-varying wave motions. In its simplest form (as given by Lundgren and Ashurst [30]), the axial vorticity and axial velocity are assumed to be uniform across the vortex core. The evolution of area-varying waves on a columnar vortex are governed by volume conservation of the core fluid, which requires that

$$\frac{d\sigma}{dt} + \frac{\sigma}{2}\frac{\partial w}{\partial z} = 0, \tag{42}$$

and by axial momentum conservation, which requires that

$$\pi\sigma^2 \frac{dw}{dt} = -\frac{\Gamma^2}{4\pi\sigma}\frac{\partial \sigma}{\partial z}, \tag{43}$$

where

$$\frac{df}{dt} \equiv \frac{\partial f}{\partial t} + w\frac{\partial f}{\partial z} \tag{44}$$

is the material derivative. Equation (43) represents a balance between the rate of change of momentum within the vortex core and the axial force due to the pressure gradient along the vortex axis, which is induced by variation of the core radius. An analytical solution of (42)–(43) for small-amplitude, axisymmetric standing waves on a vortex core can be obtained by letting

$$\sigma(z, t) = \sigma_0 + A \cos(\alpha t) \cos(kz), \tag{45}$$

where k is the wavelength and α is the oscillation frequency, and linearizing for small A/σ_0. Solution of the linearized equations yields an expression for the wave period $p = 2\pi/\alpha$ as

$$p = \frac{4\sqrt{2}\,\pi^2 \sigma_0}{k\Gamma}. \tag{46}$$

In the remainder of this section, all length, time, and velocity variables are nondimensionalized by σ_0, σ_0^2/Γ, and σ_0/Γ, respectively. For calculations with initial wave amplitude of 0.1, a standing wave forms on the vortex core which oscillates nearly periodically in time. The radial and axial velocity components within the standing wave are shown in Figs. 9a–c, using an arrow attached to each control point, for times near the beginning, middle, and end of the oscillation period. The axial motion within the standing wave is generated by oscillating azimuthal vorticity, which forms when the predominantly axial vorticity component is tilted in the azimuthal direction by an axial gradient in the swirl velocity, which arises from variation of the core radius. The core radius variation also causes a radial tilting of the vorticity vector which, in the presence of the ambient radial gradient of the swirl rate near the edge of the vortex core, also leads to accumulation of the azimuthal vorticity. In the resulting wave motion, the azimuthal vorticity magnitude attains a minimum when the slope of the core boundary is greatest and vice versa.

The average element radius during the computations was about 0.12, which yields an effective ambient vortex core radius of $\sigma_E \cong 1.12$. The theoretical oscillation period predicted from (46) with this effective radius is 39.8, whereas the period observed in the computations was about 42.3. While this agreement is fairly good, it is noted that the result (46) is approximate, since the model on which (42)–(43) are based makes several idealizations, such as uniform axial velocity profile.

Computations were also performed with a larger initial wave amplitude of 0.3. Vorticity and velocity vectors in the r–z plane for this case are shown at three different times in Figs. 10a–c and 12a–c. Contour plots of the azimuthal vorticity component are shown in Figs. 11a–c. The standing wave was observed to break up during the first oscillation, producing two traveling waves propagating in opposite directions. Numerical calculations have also been performed for the model system described by (42)–(43) using the standard MacCormack method [33], which is a second-order predictor–corrector method in which forward differencing is used on the predictor step and backward differencing is used on the corrector step. Calculations using the model equations (42)–(43) do not exhibit the bifurcation into two traveling waves observed in the direct simulations with the full vorticity collocation

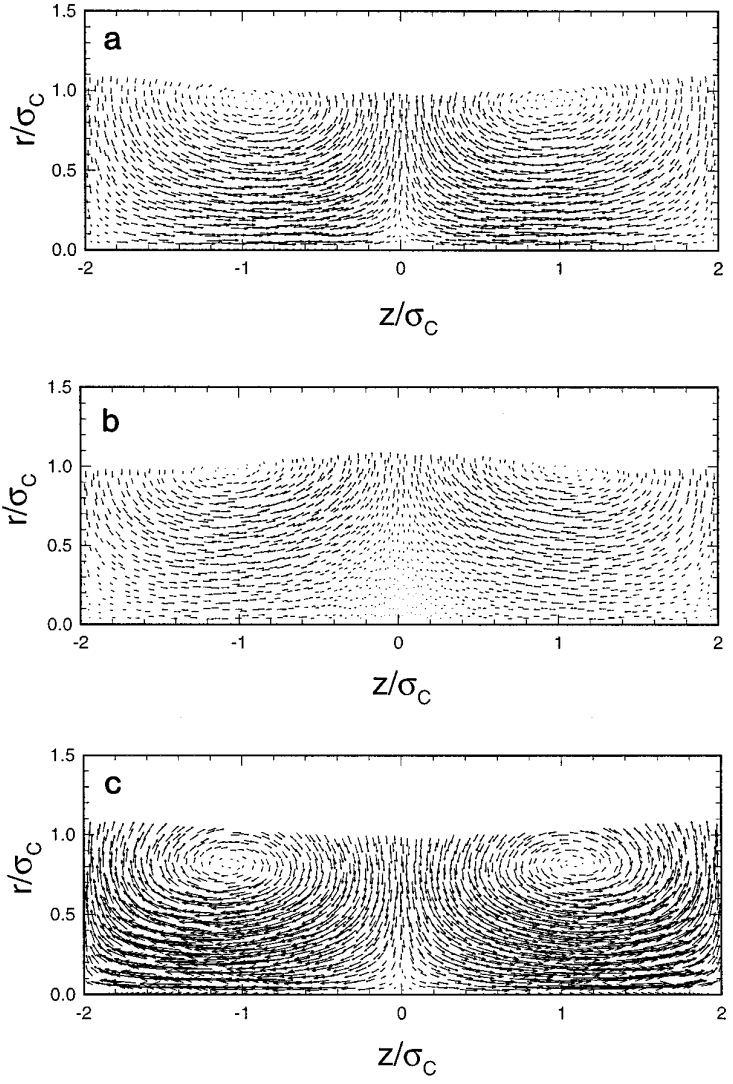

FIG. 9. Velocity vectors within a standing vortex wave with initial amplitude of 10% of the mean core radius, shown at (a) $t = 5.4$, (b) $t = 17.4$, and (c) $t = 35.4$. The wave oscillates nearly periodically in time with a dimensionless period of 42.3.

method (Figs. 10c and 12c). This difference, however, is due to the limitations of the model in [30], which (like the shallow-water model for free-surface water waves) is valid only for weakly nonlinear waves and does not account for effects of wave dispersion.

7. CONCLUSIONS

A Lagrangian vorticity collocation method was presented for axisymmetric, viscous fluid flows with or without swirl. This method has similarities to previous

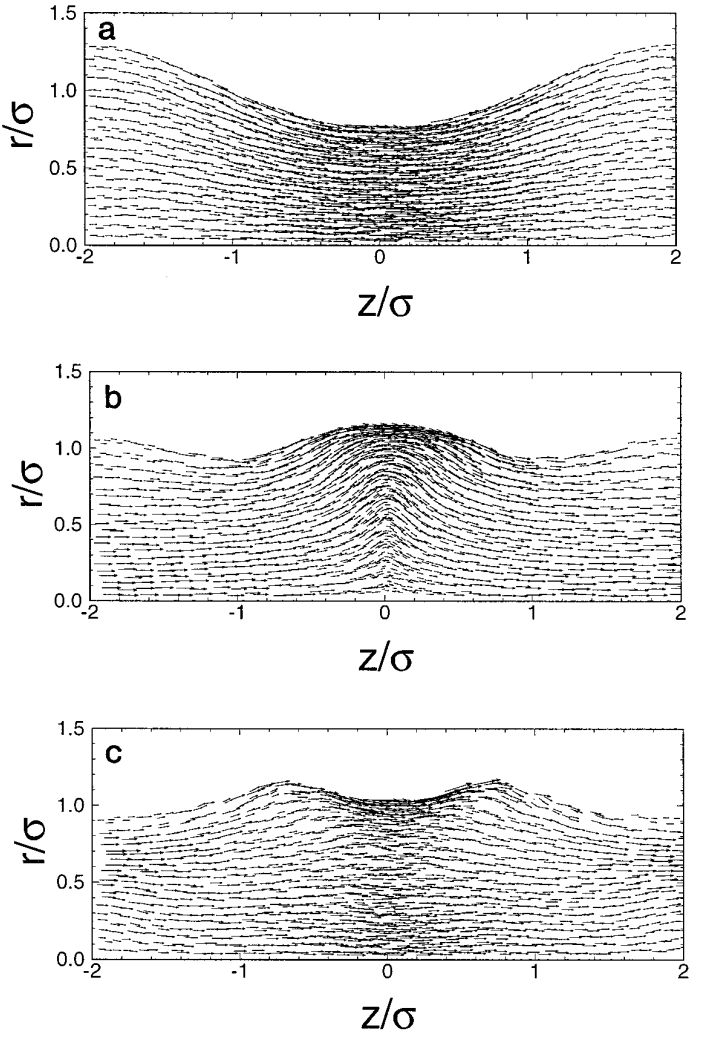

FIG. 10. Vorticity vectors in the r–z plane within a standing vortex wave with initial amplitude of 30% of the mean core radius, shown at (a) $t = 0$, (b) $t = 15.6$, and (c) $t = 31.6$. The wave bifurcates into two traveling waves, which propagate in opposite directions.

axisymmetric vortex methods [5, 6], but differs mainly in that the element amplitude is adaptively fit to the vorticity values at the control points at every time step and that the method admits both swirling and nonswirling flows. The diffusion method presented in the paper is capable of adaptively modifying the vorticity support, and the "moving least-square" differentiation method is found to maintain high accuracy even for very irregularly spaced control points. This diffusion method can be applied to arbitrary two- and three-dimensional flows with very slight changes. Both the diffusion method and the axisymmetric vortex method as a whole were subjected to a variety of validation tests, including nonswirling axisymmetric flows both far from and close to the symmetry axis, flows which evolve only through viscous

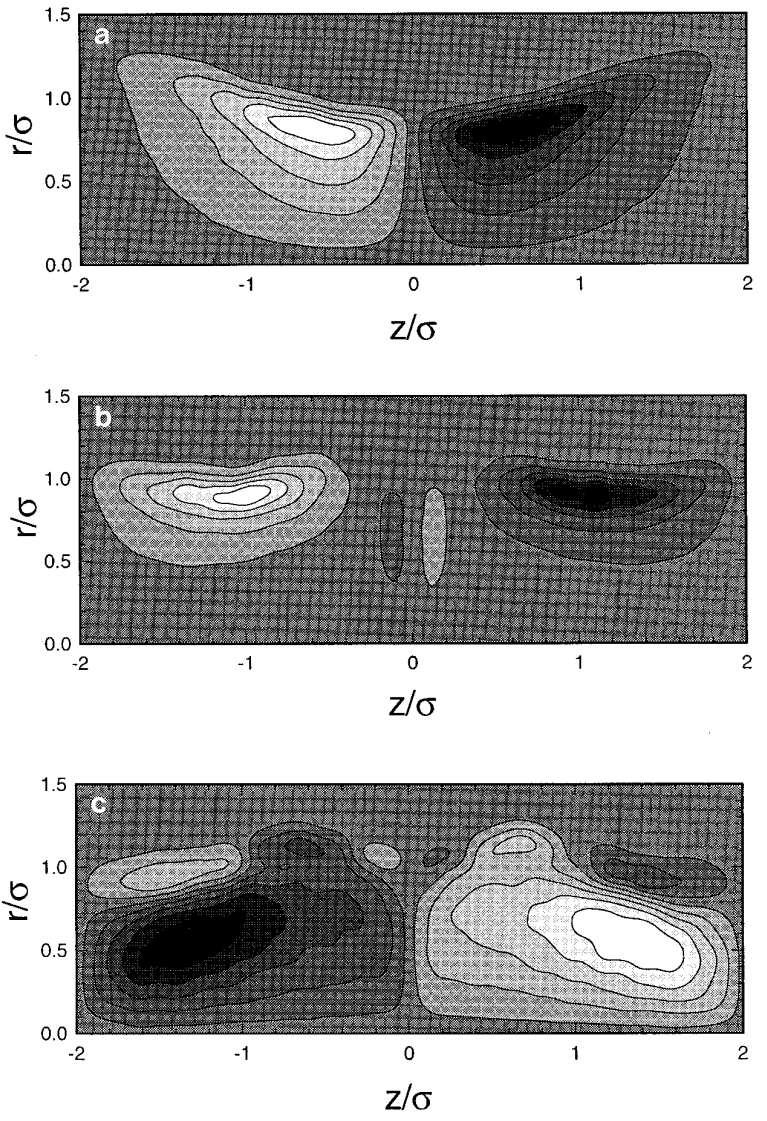

FIG. 11. Contour plots of the azimuthal vorticity component for the same cases shown in Fig. 10.

diffusion, and wave propagation in axisymmetric flows with swirl. The computed results from these validation tests were consistently found to compare well with exact solutions and with approximate solutions obtained by other means.

APPENDIX: ANALYSIS OF THE INVERSION PROCEDURE EQ. (21) IN ONE DIMENSION

In this appendix, we derive an estimate for the vorticity error caused by the iteration procedure (21) and also exemplify the filtering property of this iteration,

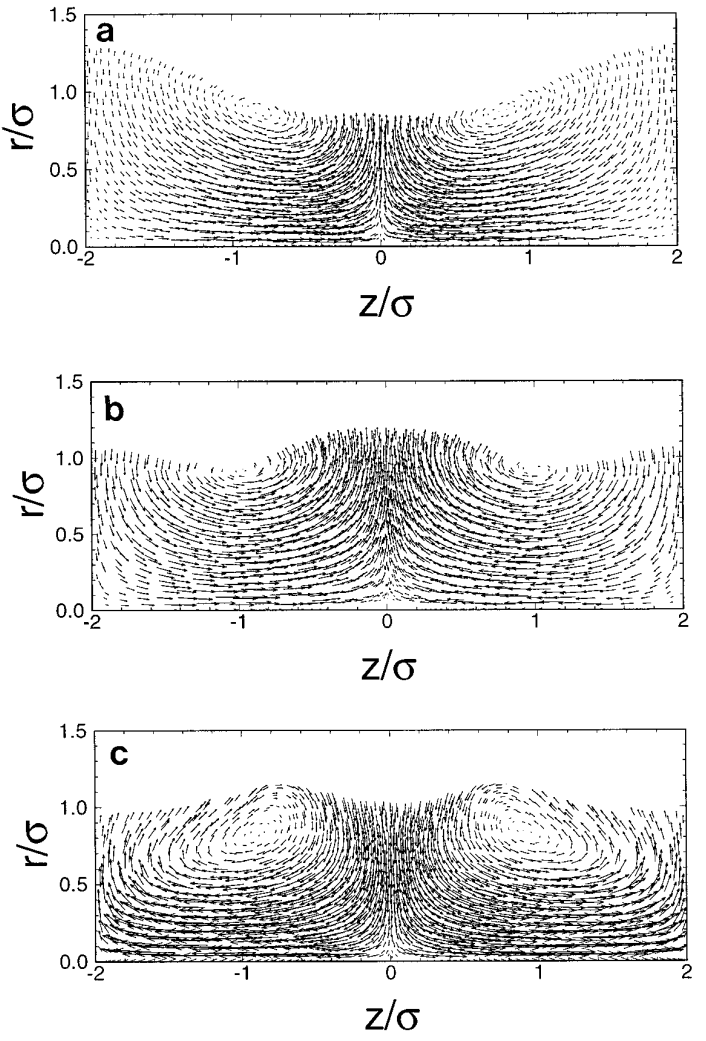

FIG. 12. Velocity vectors in the r–z plane for the same cases shown in Fig. 10.

using a continuous, one-dimensional model for the vorticity representation (5) as a convolution integral,

$$\omega(x) = \int_{-\infty}^{\infty} \Omega(x') f(x - x')\, dx'. \tag{A.1}$$

(i) *Error Analysis*

The domain of integration in (A.1) is broken up into an interval $|x' - x| \le a$ close to the point x and its complement $|x' - x| \ge a$:

$$\omega(x) = \int_{x-a}^{x+a} \Omega(x') f(x - x')\, dx' + \int_{|x'-x|\ge a} \Omega(x') f(x - x')\, dx'. \tag{A.2}$$

If it is now assumed that the function $f(x)$ is symmetric, we can use a Taylor series to expand $\Omega(x')$ about $x' = x$, together with a change in variables, to write the first integral on the right-hand side in (A.2) as

$$\int_{x-a}^{x+a} \Omega(x') f(x - x')\, dx = \Omega(x) \int_{-a}^{a} f(\xi)\, d\xi + \frac{1}{2} \frac{d^2\Omega}{dx^2}\bigg|_x \int_{-a}^{a} \xi^2 f(\xi)\, d\xi + \dots . \tag{A.3}$$

In this continuum model, the iterative procedure (21) is equivalent to setting

$$\omega(x) \cong \Omega(x) \int_{-a}^{a} f(\xi)\, d\xi + \int_{|x'-x|\geq a} \Omega(x') f(x - x')\, dx', \tag{A.4}$$

so that (A.2)–(A.4) gives the error E in the iteration procedure to leading order as

$$E = \frac{1}{2} \frac{d^2\Omega}{dx^2}\bigg|_x \int_{-a}^{a} \xi^2 f(\xi)\, d\xi. \tag{A.5}$$

For the case where $f(x)$ is a Gaussian element,

$$f(x) = \frac{1}{\delta\sqrt{\pi}} \exp(-x^2/\delta^2), \tag{A.6}$$

we have that

$$\int_{-a}^{a} f(\xi)\, d\xi = erf(a/\delta), \quad \int_{-a}^{a} \xi^2 f(\xi)\, d\xi = \frac{\delta^2}{2} P\left(\frac{3}{2}, \frac{a^2}{\delta^2}\right), \tag{A.7}$$

where $P(\cdot, \cdot)$ is the incomplete gamma function. In the limit $\delta \gg a$, neglect of the error (A.5) in comparison to the first term on the right-hand side (A.4) requires that

$$\frac{1}{3} \frac{d^2\Omega}{dx^2}\bigg|_x a^2 \ll \Omega(x). \tag{A.8}$$

In the other limit, $a \gg \delta$, neglect of this term requires that

$$\frac{1}{4} \frac{d^2\Omega}{dx^2}\bigg|_x \delta^2 \ll \Omega(x). \tag{A.9}$$

In the computations using the collocation method, the element radius is typically fit adaptively to maintain a value for the "overlap," δ/a, of approximately two. In this case, (A.2) becomes

$$\omega(x) = \Omega(x)\, \mathrm{erf}\left(\frac{1}{2}\right) + \int_{|x-x'|\geq a} \Omega(x') f(x - x')\, dx' + \frac{\delta^2}{4} P\left(\frac{3}{2}, \frac{1}{4}\right) \frac{d^2\Omega}{dx^2}\bigg|_x, \tag{A.10}$$

and the approximation (21) implies neglect of the last term in (A.10), which is of order of the square of the element radius.

(ii) *Filtering Property*

Taking the Fourier transform of the convolution integral (A.1) gives

$$\hat{\omega}(k) = 2\pi\, \hat{\Omega}(k)\hat{f}(k), \tag{A.11}$$

where a "hat" over a variable denotes the transformed variable and k is the wavenumber. Solving (A.11) for $\hat{\Omega}(k)$ and using the Gaussian (A.6) for $f(x)$, we obtain

$$\hat{\Omega}(k) = \hat{\omega}(k) \exp\left(\frac{1}{4}k^2R^2\right). \tag{A.12}$$

If $\hat{\omega}(k) \to 0$ more slowly than $\exp(-\frac{1}{4}k^2R^2)$ as $k \to \infty$, use of the exact inverse (A.12) of (A.1) indicates that $\hat{\Omega}(k)$ will become unbounded at high wavenumber. Similarly, for the discrete representation (5), exact solution of the matrix equation (20) yields values for the amplitudes which oscillate wildly between nearby control points.

Considering now the approximate representation (A.2), which corresponds to a continuous version of (21), taking the Fourier transform with the choice (A.6) for $f(x)$ gives

$$\hat{\omega}(k) = \hat{\Omega}(k)\left[\operatorname{erf}(a/R) + \exp\left(-\frac{1}{4}k^2R^2\right)\right. \tag{A.13}$$
$$\left.\left\{1 - \frac{1}{2}\operatorname{erf}\left(\frac{a}{R} + \frac{1}{2}kRi\right) - \frac{1}{2}\operatorname{erf}\left(\frac{a}{R} - \frac{1}{2}kRi\right)\right\}\right].$$

The expression (A.13) gives a high wavenumber asymptotic expression for $\hat{\Omega}(k)$ as

$$\hat{\Omega}(k) \sim \frac{\hat{\omega}(k)}{\operatorname{erf}(a/R)} \quad \text{as } kR \to \infty, \tag{A.14}$$

whereas the solution for $\hat{\Omega}(k)$ from (A.13) approaches that given in (A.12) as $kR \to 0$. We thus find that the approximation (A.12) acts to force the amplitude function $\hat{\Omega}(k)$ to zero at high wavenumbers, provided only that $\hat{\omega}(k) \to 0$ as $k \to \infty$ (i.e., that $\omega(x)$ is sufficiently smooth). This result, applied to the discrete version of (A.1), confirms our empirical observations that the iteration (21) acts to filter out oscillations in amplitude occurring on a length scale much less than the element radius.

ACKNOWLEDGMENT

Research support for JSM was provided by the U.S. Army Research Office under Grant DAAH04-96-1-0081 (Thomas Doligalski, program manager) with the University of Iowa. Research support for JRG was provided by the U.S. Office of Naval Research under Grant N0001494WX35105 (James Fein, program officer) and by internal funding from the Naval Undersea Warfare Center, Division Newport. Computer time for JSM was provided by a grant from the San Diego Supercomputing Center.

REFERENCES

1. A. Pumir and E. D. Siggia, Development of singular solutions to the axisymmetric Euler equations, *Phys. Fluids A* **4**(7), 1472 (1992).
2. A. Landsberg and E. Murman, Control of numerical diffusion in computational modeling of vortex flows, *Prog. Astronaut. Aeronaut.* **146,** 205 (1991).
3. A. Leonard, Computing three-dimensional incompressible flows with vortex elements, *Ann. Rev. Fluid Mech.* **17,** 523 (1985).
4. E. Meiburg, Three-dimensional vortex dynamics simulations, in *Fluid Vortices*, edited by S. I. Green (Kluwar Academic, Dordrecht, 1995), p. 651.
5. E. Acton, A modelling of large eddies in an axisymmetric jet, *J. Fluid Mech.* **98,** 1 (1980).
6. J. H. Strickland and D. E. Amos, Fast solver for systems of axisymmetric ring vortices, *AIAA J.* **30,** 737 (1992).
7. J. Carrier, L. Greengard, and V. Rokhlin, A fast adaptive multipole algorithm for particle simulations, *SIAM J. Sci. Statist. Comput.* **9**(4), 669 (1988).
8. J. T. Beale, On the accuracy of vortex methods, *Proc. Workshop on Comput. Fluid Dyn. & Reacting Gas Flows, I.M.A., Univ. Minnesota, 1986.*
9. J. S. Marshall and J. R. Grant, Penetration of a blade into a vortex core: vorticity response and unsteady blade forces, *J. Fluid Mech.* **306,** 83 (1996).
10. D. Fishelov, A new vortex scheme for viscous flows, *J. Comput. Phys.* **86,** 211 (1990).
11. P. Degond and S. Mas-Gallic, The weighted particle method for convection-diffusion equations. Part 1. The case of an isotropic viscosity, *Math. Comput.* **53,** 485 (1989).
12. J. S. Marshall and J. R. Grant, A Lagrangian collocation method for vorticity transport in viscous fluid flows, in *Proc. of the Forum on the Application of Vortex Methods to Engineering Problems, Albuquerque, New Mexico, Feb. 22–24, 1995.*
13. P. Koumoutsakos, A. Leonard and F. Pépin, Boundary conditions for viscous vortex methods, *J. Comput. Phys.* **113,** 52 (1994).
14. P. S. Bernard, A deterministic vortex sheet method for boundary layer flow, *J. Comput. Phys.* **117,** 132 (1995).
15. Y. Ogami and T. Akamatsu, Viscous flow simulation using the discrete vortex model—The diffusion velocity method, *Comput. & Fluids* **19,** 433 (1991).
16. S. N. Kempka and J. H. Strickland, *A Method to Simulate Viscous Diffusion of Vorticity by Convective Transport of Vortices at a Non-solenoidal Velocity,* Sandia Natl. Lab. Tech. Rep. SAND93-1763 (1993).
17. I. S. Gradshteyn and I. M. Ryzhik, *Tables of Integrals, Series and Products* (Academic Press, Orlando, FL 1980).
18. C. M. Bender and S. A. Orszag, *Advanced Mathematical Methods for Scientists and Engineers* (McGraw-Hill, New York, 1978).
19. P. G. Saffman, The velocity of viscous vortex rings, *Stud. Appl. Math.* **49,** 371 (1970).
20. M. Abramowitz and I. A. Stegun, *Handbook of Mathematical Functions* (Dover, New York, 1965).
21. W. H. Press, W. T. Vettering, S. A. Teukolsky, and B. P. Flannery, *Numerical Recipes in FORTRAN*, 2nd ed. (Cambridge Univ. Press, New York, 1992), Chap. 18.
22. A. J. Chorin, A numerical study of slightly viscous flow, *J. Fluid Mech.* **57,** 785 (1973).
23. A. F. Ghoniem and F. S. Sherman, Grid-free simulation of diffusion using random walk methods, *J. Comput. Phys.* **61,** 1 (1985).
24. J. H. Ferziger and M. Peric, *Computational Methods for Fluid Dynamics* (Springer-Verlag, Berlin, 1996), p. 48.
25. Lord Kelvin, The translatory velocity of a circular vortex ring, *Phil. Mag.* **33,** 511 (1867).
26. M. J. M. Hill, On a spherical vortex, *Phil. Trans. Roy. Soc. Lond. A* **185,** 213 (1894).

27. H. K. Moffatt and D. W. Moore, The response of Hill's spherical vortex to a small axisymmetric disturbance, *J. Fluid Mech.* **87,** 749 (1978).
28. C. Pozrikidis, The nonlinear instability of Hill's vortex, *J. Fluid Mech.* **168,** 337 (1986).
29. J. Norbury, A family of steady vortex rings, *J. Fluid Mech.* **57,** 417 (1973).
30. T. S. Lundgren and W. T. Ashurst, Area-varying waves on curved vortex tubes with application to vortex breakdown, *J. Fluid Mech.* **200,** 283 (1989).
31. J. S. Marshall, A general theory of curved vortices with circular cross-section and variable core area, *J. Fluid Mech.* **229,** 311 (1991).
32. A. Leonard, Nonlocal theory of area-varying waves on axisymmetric vortex tubes, *Phys. Fluids* **6,** 765 (1994).
33. R. Peyret and T. D. Taylor, *Computational Methods for Fluid Flow* (Springer-Verlag, New York, 1990).